Effect of rapid thermal annealing on damage of silicon matrix implanted by low-energy rhenium ions

I.N. Demchenko, Y. Melikhov, M.S. Walczak, R. Ratajczak, K. Sobczak, A. Barcz, R. Minikaev, E. Dynowska, J.Z. Domagala, M. Chernyshova, Y. Syryanyy, N.V. Gavrilov, M. Sawicki

PII: S0925-8388(20)32797-3

DOI: https://doi.org/10.1016/j.jallcom.2020.156433

Reference: JALCOM 156433

To appear in: *Journal of Alloys and Compounds*

Received Date: 22 April 2020

Revised Date: 14 July 2020

Accepted Date: 15 July 2020

Please cite this article as: I.N. Demchenko, Y. Melikhov, M.S. Walczak, R. Ratajczak, K. Sobczak, A. Barcz, R. Minikaev, E. Dynowska, J.Z. Domagala, M. Chernyshova, Y. Syryanyy, N.V. Gavrilov, M. Sawicki, Effect of rapid thermal annealing on damage of silicon matrix implanted by low-energy rhenium ions, *Journal of Alloys and Compounds* (2020), doi: https://doi.org/10.1016/j.jallcom.2020.156433.

CRediT authorship contribution statement

IN Demchenko: Conceptualization, Methodology, Project administration, Validation, Visualization, Formal analysis, Writing - original draft, Supervision, Writing - review & editing. **Y Melikhov:** Conceptualization, Methodology, Formal analysis, Visualization, Writing - review & editing. **MS Walczak:** Validation, Investigation, Visualization. **R Ratajczak:** Formal analysis, Writing - review & editing. **K Sobczak:** Data curation, Investigation, Validation, Writing - review & editing. **A Barcz:** Data curation, Validation. **R Minikaev:** Formal analysis, Validation, Investigation, Visualization, Writing - review & editing**. E Dynowska:** Formal analysis, Validation, Visualization. **JZ Domagala:** Formal analysis, Validation, Visualization. **M Chernyshova:** Formal analysis, Investigation, Writing - review & editing. **Y Syryanyy:** Data curation, Investigation, Visualization. **NV Gavrilov:** Resources, Validation, Writing - review & editing. **M Sawicki:** Investigation, Writing - review & editing.

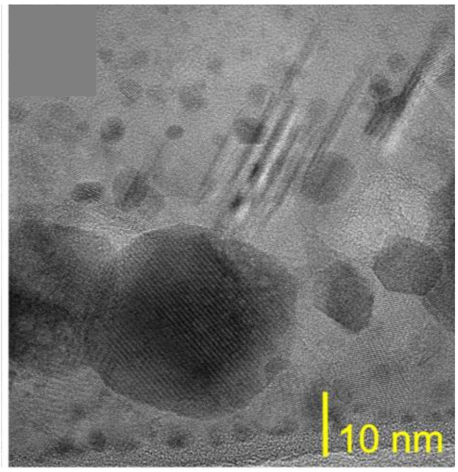
10 nm

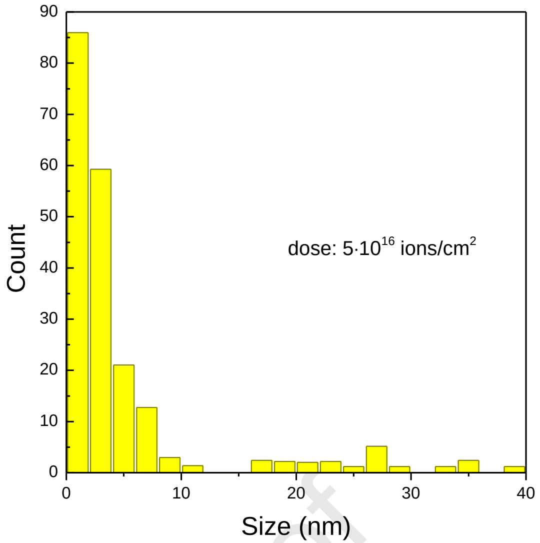
Count
Size (nm)
dose: 5·10^16 ions/cm^2
0
10
20
30
40
50
60
70
80
90
0
10
20
30
40

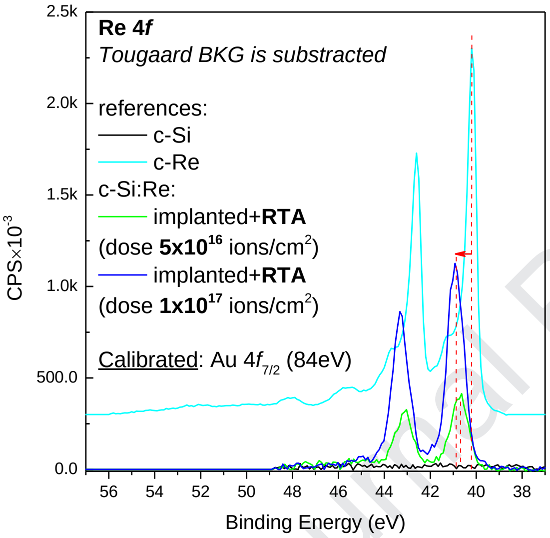
Re 4f
Tougaard BKG is substracted
references:
c-Si
c-Re
c-Si:Re:
implanted+RTA
(dose 5x10^16 ions/cm^2)
implanted+RTA
(dose 1x10^17 ions/cm^2)
Calibrated: Au 4f7/2 (84eV)
CPS×10^-3
Binding Energy (eV)
0.0
500.0
1.0k
1.5k
2.0k
2.5k
56
54
52
50
48
46
44
42
40
38

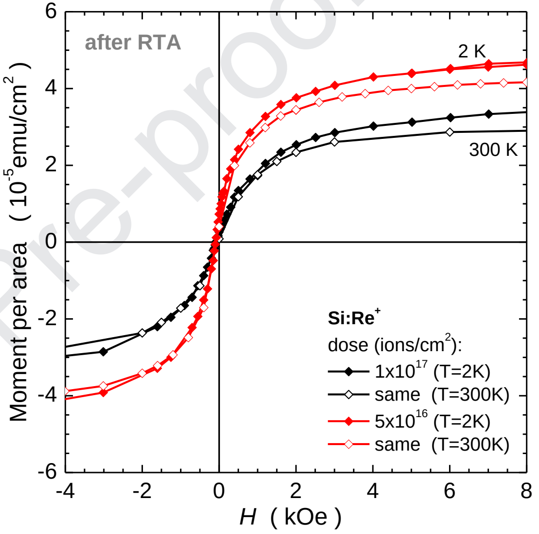
after RTA
2 K
300 K
Si:Re+
dose (ions/cm^2):
1x10^17 (T=2K)
same (T=300K)
5x10^16 (T=2K)
same (T=300K)
Moment per area (10^-5emu/cm^2)
H (kOe)
-6
-4
-2
0
2
4
6
-4
-2
0
2
4
6
8

Effect of rapid thermal annealing on damage of silicon matrix implanted by low-energy rhenium ions

IN Demchenko*[a], Y Melikhov[b], MS Walczak[c], R Ratajczak[d], K Sobczak[e], A Barcz[f], R Minikaev[f], E Dynowska[f], JZ Domagala[f], M Chernyshova[g], Y Syryanyy[d], NV Gavrilov[h] and M Sawicki[f]

[a] University of Warsaw, Department of Chemistry, ul. Pasteura 1, 02-093 Warsaw, Poland
[b] School of Engineering, Cardiff University, Cardiff, CF24 3AA, United Kingdom
[c] Corrosion & Protection Centre, School of Materials, The University of Manchester, Sackville Street, The Mill, Manchester, M1 3BB, United Kingdom
[d] National Centre for Nuclear Research, A. Soltana 7, 05-400 Otwock-Swierk, Poland
[e] Faculty of Chemistry, Biological and Chemical Research Centre UW, Żwirki i Wigury 101, 02-089 Warsaw, Poland
[f] Institute of Physics, Polish Academy of Sciences, Lotnikow Alley 32/46, 02-668 Warsaw, Poland
[g] Institute of Plasma Physics and Laser Microfusion, Hery Street 23, 01-497 Warsaw, Poland
[h] Institute of Electrophysics, Ural Branch, Russian Academy of Sciences, Yekaterinburg, Russia

Abstract

The structural, electronic, and magnetic properties of low-energy rhenium implanted c-Si are examined for the first time. The damage created by rhenium ions and the following partial reconstruction of the silicon host matrix after rapid thermal annealing (RTA) are investigated as a function of the fluence. Rutherford backscattering spectrometry (RBS) results reveal that the implanted ions are located in the near-surface region with the distribution maximum at about 23 nm below the surface. The analysis of rhenium-depth distribution using the McChasy code shows that the implanted Re-ions are located in the interstitial lattice positions. The RTA leads to a partial recovery of the silicon crystal structure. According to the RBS results, the formed inclusions are not coherent with the silicon host matrix causing an increase of the lattice distortion. Analysis of channeled RBS/c spectra carried out by the McChasy code revealed different levels of bent channels in damaged regions suggesting bimodal distribution of inclusions in the silicon. Studies of high-resolution X-ray photoelectron spectroscopy (XPS) conducted after the RTA showed the shift of Re $4f_{7/2}$ binding energy (BE) by +0.68 and +0.85 eV with respect to metallic rhenium for the samples with lower/higher fluencies, respectively. Complex XPS, density functional theory (DFT) simulations, and transmission electron microscopy (TEM) data analysis allowed us to conclude that the near-surface layer of the sample (~10 nm) consists of nanoinclusions with cubic and/or hexagonal ReSi. In the middle area of the samples, much larger nanoinclusions (> 10/20 nm for higher/lower fluencies, respectively) containing pure metallic rhenium inside are formed. The RTA increases the magnetic moment of the sample with the lower dose nearly 20-fold, whereas in the sample with the higher dose a 3-fold increment is observed only. The magnetic response of the examined systems after the RTA indicates a presence of magnetic interactions between the nanoinclusions resulting in the system exhibiting super-spin glass or super-ferromagnetism.

Keywords: Rhenium-implanted Silicon, RBS, XPS, RTA, TEM, DFT.
**Corresponding author:* idemchenko@chem.uw.edu.pl

1. Introduction

In addition to electron charge, spintronics utilizes spin as another degree of freedom [1]. Some metal-based spintronic devices have been realized already but incorporation of magnetic properties into *semiconductors*, that are widely used in electronics, will truly open up new possibilities [2]. An obvious critical requirement for these materials is to possess ferromagnetism at room temperature or above. Another critical requirement is to exhibit stable single-phase magnetic semiconductor properties [3]. An obvious choice is to take pure group IV elements (Si or Ge) or to use either II-VI or III-V semiconducting systems as a base and introduce 3*d* transition metal atoms into it. There are plenty of successful examples: (Ga,Mn)As [4], (Ga,Mn)N [5], $Si_{1-x}Mn_x$ [6], $Si_{1-x}Co_x$ [7], Mn_xGe_{1-x} [8], $Si_{1-x}Cr_x$ [9], and many-many others, however only a low temperature single magnetic phase materials have been realized [10].

Contrary to the doping by 3*d* series transition metals, the experimental studies of group IV elements doping by 4*d* and 5*d* transition metals are relatively rare with magnetic properties not investigated at all. This is due to the fact that these studies are rather oriented towards creating an intermediated band in order to improve photoresponse of silicon to be used in photovoltaics (e.g., see [11, 12] and references therein). Theoretical studies oriented towards understanding and improvement of such systems are even rarer. In fact, to the best of the authors' knowledge, the only research related to the analysis of properties of group IV semiconductors doped by 5*d* transition metal was presented in [13-15], where the electronic structure and stability of a single Re impurity in silicon and of a pair of substitutional and/or interstitial Re impurities were investigated theoretically by means of density functional theory (DFT), which also allowed analysis of temperature dependence of magnetization of these systems.

In those studies, it was predicted that the most stable position of Re in an undoped Si is the substitutional site with the local magnetic moment of 1 μ_B [13]. This led to a conclusion that, as opposed to doping with Mn that prefers occupying interstitial sites, doping with Re should lead to a more stable positioning of impurities and, therefore, should prevent Re from agglomerating [13]. In case of co-presence of substitutional and interstitial impurities of Re, it was found that it was energetically favorable for them to form pairs. These pairs, however, make the system nonmagnetic due to a charge transfer between the impurities. Magnetic properties can be restored by charge co-doping of *n*-type being more efficient than *p*-type [14]. In case of substitutional impurities of Re only, theoretical calculations predicted an increase of Curie temperature with increase of concentration of impurities achieving Curie temperatures well above room temperature for Re concentration higher than 3% [15]. Overall, those predictions highlighted a possibility of building a stable magnetic semiconductor out of group IV elements with Curie temperature well above room temperature and, at the same time, emphasized important factors and their effects on final properties of Si doped by Re in terms of the purity and type of charge doping of Si to be avoided during production.

These theoretical results are valuable from the application point of view. In that context, a question of choosing the reasonable method to obtain such structures has to be answered. Generally, there is a number of experimental methods that can be used to dope transition metals into semiconductor systems. Molecular beam epitaxy (MBE) [8, 16, 17] and ion implantation [6, 7, 18] are the most frequently used techniques in the semiconductor industry. The usage of other techniques, such as magnetron sputtering [9, 19] or surface-based integration of metal into a host [20, 21], is not so extensive. The main drawback of ion implantation is its rather uncontrollable nature resulting in a very inhomogeneous system: dopant ions could frequently occupy substitutional and/or interstitial positions, form phase separation, and produce defects in the host lattice - all these factors have an impact on magnetic properties [22]. Nevertheless, in case of Re dopant, ion implantation seems to be the only choice as usage of MBE in this case [23, 24] is difficult due to extremely high melting temperature of Re [25]. Moreover, it is worth noting that some transition metals cannot be dissolved in silicon at high enough concentration (usually at about 1 up to 10 at.%) that is essential for spintronic applications. For instance, manganese has a maximum solubility of ~10^{16}/cm^2 in crystalline silicon [26].

To the best of the authors' knowledge this is the first thorough experimental study of Re doped Si, with the only found hint mentioned by Wierzbowska [14, 15] about a slightly different system: "amorphous silicon doped with rhenium has been experimentally observed to be ferromagnetic at room temperature; however, this phenomenon disappears when samples stay in ambient conditions for a few months [R.R. Galazka et al. (private communication)]."

In this work, the electronic and crystallographic structures of Re-ion implanted silicon before and after rapid thermal annealing (RTA) are studied using RBS/c, XPS, XRD, TEM techniques. The XPS measurements of core-levels are complemented with DFT calculations. Finally, the magnetic response of the obtained system is investigated.

2. Material and methods

2.1 Samples preparation

Silicon wafers (100) were implanted with Re-ions having 30 keV energy at room temperature. The sample lateral size was 1×0.5 cm^2. Overall, two samples were produced: hereafter the sample with a lower implantation dose (fluence 5×10^{16} cm^{-2}) will be referred to as Si:Re16 and the sample with a higher implantation fluence 1×10^{17} cm^{-2}, as Si:Re17. Rhenium ion source cathode 8 mm diameter and 10 mm height was pressed from powder of reduced rhenium (brand Re-1 powder with mean grain size of 3.0 microns and mass fraction of Re 99.9% was manufactured by "PROMELEKTRONIKA CJSC", prosp. 50 Let Oktyabrya 108/50A, Saratov, 410040, Russia). Magnetic-pulse compression of cathode was conducted under vacuum at a temperature of 425°C. Before implantation, the vacuum in work chamber was at 4×10^{-5} Torr level. Pressure of argon in the work chamber during irradiation was 2×10^{-4} Torr. The pumping was carried out using oil-free turbo-molecular pump Varian TV 3 KT. Subsequent ion irradiation was performed employing the pulsed mode with pulse duration of 0.4 ms and frequency of 25 Hz. The current density of the beam during the pulse was kept below 0.8 mA/cm^2. After implantation, the samples were remained in the high vacuum conditions for 20 min. Ion implantation was performed using modified MEVVA (Metal Vapor Vacuum Arc) ion source with gas discharge ignition. The standard MEVVA ion source requires a discharge over the dielectric surface to initiate the arc to the metal cathode, ions of which are required. The modified MEVVA ion source on the other hand, initiates the required arc via auxiliary gas discharge in argon. This leads to presence of argon impurities in the ion beam, though relatively insignificant (less than 10%). This modification was realized to increase the service life of the ignition system (refer to [27] for further details regarding the used ion source system).

After initial study was finished, the samples were subjected to a post-implantation RTA in Ar gas at $T_A = 1000\ ^{\circ}C$ for 60 s. The samples after the RTA are referred to as Si:Re16R and Si:Re17R in the manuscript to distinguish them from the samples before the RTA. Pure silicon and rhenium references (marked c-Si and h-Re) were also used during characterization of investigated samples.

2.2 Rutherford backscattering spectrometry

A NEC 3SDH-2 Tandem Pelletron accelerator was used to measure thicknesses and compositions of the investigated samples by RBS exploiting the channeling mode (RBS/c). The method is based on directing a well-collimated beam of 2 MeV helium ions into a sample and recording the energy spectra of the backscattered ions. The orientation of the sample with respect to the incident ion beam was varied to align the incident beam with the crystalline axis near normal to the silicon wafer and, thus, exploiting the larger difference in channeled RBS yield between crystalline and amorphous silicon.

2.3 X-ray photoelectron spectroscopy

The samples were studied by XPS using a Kratos Ultra Axis spectrometer with monochromatic Al Kα radiation (hν = 1.4866 keV) from an X-ray source with a spot of $700\times300\ \mu m^2$ (due to the analyzer settings in hybrid mode) while operating at 150 W and 15 kV. The high-resolution (HR) XPS spectra were collected with the hemispherical analyzer at the pass energy of 20 eV and the energy step size of 0.1 eV. The photoelectron take-off angles were 0, 25, 45, and 60° with respect to the normal to the sample's surface plane. An analyzer acceptance angle was ±7°. No charge compensation was applied. Samples were mounted on the grounded holder. Binding energies (BEs) of the photoelectrons were calibrated using the Au $4f_{7/2}$ photoelectron peak at 84 eV. The CasaXPS software (version 2.3.17) [28] was used to evaluate the XPS data.

Taking into account that sputtering procedure can easily modify electronic structure of studied samples due to intermixing of atoms (see, e.g., [29]), it was decided to abandon sputtering in this study. Consequently, before the RTA procedure, the surface of the samples was cleaned by wet chemistry. The etchant was a concentrated Hydrofluoric acid (47-51%) supplied by Fisher Chemicals mixed with deionized (DI) water (15 M Ohm) with the ratio of 1:9 (4:36 ml). The samples were immersed in the etchant one at a time and gently agitated for 20 seconds. After that, they were rinsed in DI water for 30 seconds. This procedure was not applied to the samples after the RTA.

In order to decrease the amount of native oxides at the surface of the rhenium reference sample (marked h-Re), it was annealed at $1050\ ^{\circ}C$ for 30 min.

2.4 X-ray diffraction

The XRD measurements were carried out by modern laboratory Bragg-Brentano diffractometer (X´Pert Pro Alpha1 MPD, Panalytical) equipped in Johansson primary Ge (111) monochromator and semiconductor linear position-sensitive detector. The 2θ - θ diffraction patterns were collected in $20 – 65^{\circ}\ 2\theta$ range using the Cu $K_{\alpha1}$ radiation.

2.5 Scanning transmission electron microscopy

The conventional and high-resolution STEM observations were performed with TALOS F200XFEI system, operating at 200 kV. High angle annular dark field (HAADF) imaging was combined with the energy-dispersive x-ray spectroscopy (EDS). Selected area electron diffraction (SAED) was used to identify crystal structures.

2.6 Magnetic measurements

The magnetic measurements were performed in a Quantum Design MPMS 7 T superconducting quantum interference device (SQUID) magnetometer equipped with a low field option, and following strictly the guidelines of precise magnetometry of thin layers on a substrate [30]. All magnetic measurements were carried out using about ~20 cm long silicon strips to fix the samples in the magnetometer and the adequate experimental code for minute signals measurements was strictly observed [30]. By design, the signal detection axis is aligned with the direction of the magnetic field H (vertically), recording the vertical component of the magnetization vector only. Special care was taken towards screening the sample from external magnetic fields, and to keep the parasitic remnant fields generated by the magnet at the lowest possible level. Using a test sample of a paramagnetic Dy_2O_3, a magnitude of H acting on the sample after magnet degaussing procedure has not been established to stay below 0.15 Oe. Magnetic moment as a function of H was recorded at 2 K and 300 K.

2.7 DFT calculations

Ab-initio calculations of the electronic structure were performed using the full-potential linearized-augmented-plane-wave + local orbitals (FLAPW-lo) method utilized in the WIEN2k code [31]. The exchange-correlation functional was chosen to be Perdew-Burke-Ernzerhof (PBE) potential within the generalized gradient approximation (GGA) [32]. In all models, the muffin-tin (MT) sphere radii were chosen to be 2.5 a.u. for Re and 2.19 a.u. for Si. In the MT spheres, the l-expansion of the non-spherical potential and charge density were set up to $l_{\max} = 10$. In order to achieve energy eigenvalues convergence, the basis function up to $R_{MT}K_{MAX} = 7$ was used, where K_{MAX} is the maximum modulus of the reciprocal lattice vector and R_{MT} is the average radius of the MT spheres. The charge density was truncated at $G_{MAX} = 12$ bohr^{-1}. The hexagonal unit cell of rhenium with $a = b = 2.7608$ Å, $c = 4.4582$ Å (space group P6$_3$/mmc) was chosen as a base for all the models except for c-ReSi for which cubic unit cell (space group P$_{21\ 3}$, $a = b = c = 4.775$ Å) was applied. In order to fine-adjust the chemical composition of the structure, as well as to minimize an influence of a core-hole created on one of Re atoms, a supercell having 54 and 64 atoms in a 3×3×3 unit cell was created for h-ReSi and c-ReSi, respectively. A convergence test with respect to the k-points was performed identifying a sufficient number of irreducible k-points as 150. The energy convergence limit for the self-consistent iterations was set to 10^{-4} Ry. The separation of the valence and core states was made selecting the localization criterion to be equal 0.999 instead of explicitly stating the energy of separation. That allowed putting Re 4f states straight into the core and in this case spin-orbit coupling is included nearly exactly.

Binding energies of Re 4f were obtained using a "half-core hole" approximation based on Slaters transition state theory that predicts a fairly accurate absolute energies as opposed to the one-electron approximation that underbinds the core levels [33]. As the name of the approximation states, half-core hole has to be created for a desired state. The XPS value of the peak position is a difference between Fermi energy E_F and the energy of that selected state obtained from the self-consistent calculations. As a state of interest, Re 4$f_{7/2}$ was chosen.

3. Results and discussion

3.1 RBS investigations supported by SRIM and McChasy simulations

The projected depth of 30 keV Re in silicon target was estimated to be around 23 nm using the Stopping and Range of Ions in Matter (SRIM) software based on a quantum mechanical treatment of ion-atom collisions [34] (see **figure S1** (a, c) in Supplementary Material). The SRIM Monte Carlo simulations were used to calculate the density of energy deposition as a function of depth for each incident ion with all recoil collisions, both primary and secondary, as these collisions produce vacancies in the host matrix (silicon). This quantity is referred here as the recoil energy density E_R, expressed in eV/Å per incident ion. Multiplying E_R by the dose D of implanted ions (ions/cm^2), one can obtain a value for the total energy density E_d invested in damage creation during a particular implantation run, i.e. $E_d = E_R \times D$ being expressed in eV/cm^3. In [35] it was proposed that E_d at a given depth d should scale with the degree of disorder produced in silicon, up to some particular “threshold” value of E_d at which amorphization is essentially complete, as indicated experimentally by total loss of channeling in RBS (see **figure 1** (a, b)). The depth of totally amorphized layer may then be estimated as a position of intersection of the threshold line with E_d depth distribution curve. Using a threshold level of 5×10^{23} eV/cm^3, i.e. a value for silicon estimated in [35], the depths of a complete amorphization were estimated to be 36 and 38 nm for the lower and higher implantation doses, respectively (see **figure S1** (b) in Supplementary Material). It is important to note that the SRIM model is applicable only when implantation is performed at or below LN_2 temperatures, i.e. at temperatures for which vacancy mobility is low. Despite this, the subsequent analysis of XPS data leads to a conclusion that even such a rough estimation is sufficient to explain visible modification of electronic structure (namely Si 2p states) of investigated samples. We will come back to this issue during our analysis/interpretation of the XPS data.

Figure 1 shows random and channeling RBS spectra obtained for the samples with lower and higher doses of implantation prior to and after the RTA. As a reference, the random and channeling spectra for the virgin Si are included. As it was mentioned earlier, the mean projected range of 30 keV Re ions in c-Si was found to be at 23 nm. Analysis of the Re-depth distributions using the McChasy simulation [36], that also uses the Monte Carlo approach, is consistent with the results obtained by the SRIM (see **figure S1 (c)** in Supplementary Material). As was expected, the implantation process produced a lattice damage in the region with the depth that corresponds to the ion range (see **figure S1 (a, b)** in Supplementary Material). Analysis of the RBS spectra before the RTA in **figure 1** reveals that the intensity of Si signals in the aligned spectra is practically at the level of the random ones. It means that after the implantation the amorphization of the crystal structure takes place. At deeper range, the RBS yield is reduced due to a partial channeling of ions that emerge from the amorphous layer into the undamaged silicon below (dechanneling). As suspected for higher fluence, the amorphized layer became somewhat thicker (that is clearly seen in the inset in **figure 1 (a)**) due to the amorphization threshold of the deposited energy being positioned deeper for a higher fluence (see **figure 1 (b)**). As for the Re-signal, it is similar for both aligned and random spectra. This is a clear indication that the implanted Re atoms are located in the interstitial lattice positions.

The RTA treatment leads to a partial recovery of the crystal structure (see **figure 1 (a, b)**): for both samples the changes of structural defects depth distributions can be observed (marked by arrows), whereas the Re-depth distributions remain unchanged. Supposedly, the depth contribution of the implanted species is affected by the out-diffusion process. The aligned spectra reveal double damage feature near 1100 eV (the inset in **figure 1 (b)** shows this clearer for both samples). That means that two different regions of defects are created after annealing with the recovered Si layer between them. As it will be shown further, it is related to cluster formations in the Si host matrix. The clusters are not aligned with the silicon host matrix causing an increase of the lattice distortion and, hence, an increase in dechanneling yield. Noteworthy, the analysis of the channeled RBS spectra carried out using the McChasy simulation code [36] reveals different levels of bent channels in defects regions (see **figure 1 (d)**). The difference in levels clearly suggests that clusters formed in these regions are different in size. Also, the number of formed clusters is larger for higher fluence and bent channels are much stronger. In addition, it cannot be excluded that inclusions of Re:Si phases (silicides) are formed, thus perturbing the silicon crystalline structure.

3.2 XPS studies of Si 2p and Re 4f states before RTA treatment

The HR XPS Si 2*p* spectra of reference c-Si and Re-implanted silicon samples before the RTA are shown in **figure 2** (a). For all the samples, an oxygen contamination was found to be present at the outermost surface (marked as "Si 2*p* oxides" in **figure 2** (a)). To determine the chemical nature of silicon states, the Si 2*p* spectra were de-convoluted after a subtraction of a 'U Si Tougaard' background, taking the Gaussian-Lorentzian shape curves of 30% Lorentzian character. Particular details of the model and de-convolution procedure could be found in [29]. The spin-orbit splitting (Si $2p_{3/2}$ and Si $2p_{1/2}$ peaks are separated by 0.63 eV) is visible for the right-hand peak corresponding to elementary silicon $\mathrm{Si}^{(el.)}$. After the implantation, the peak-width of $\mathrm{Si}^{(el.)}$ increases gradually, so the separation of the doublet becomes unclear. Moreover, a shift of the main line by 0.37 eV towards lower values of binging energy relative to the $\mathrm{Si}^{(el.)}$ position is clearly observed in **figure 2** (a). It is assumed that both visible shift and broadening of the peak point out to formation of highly damaged, close to amorphous, regions. They extend from the sample's surface and are formed as a result of the implantation. As it was found in [37], the deviations in the bond length and bond angle distributions from those values in the crystalline silicon lead to the valence electron charge distribution fluctuations between c-Si and a-Si, thus they could be responsible for modification of Si 2*p* states observable in **figure 2** (a). Our hypothesis concerning amorphization/(high disorder) is supported by the RBS investigations and SRIM simulations presented above, as well as XRD and TEM investigations that will be discussed in the sections below. Additionally, the results presented in [38] where 'in situ' analysis of Si (100) surface damage induced by low-energy rare-gas ion bombardment using XPS was performed, support this hypothesis as well. Particularly, it was found that a-Si layer with a uniform thickness *is formed* by the dosage of rare-gases (Ne, Ar, or Xe) at the level of 10^{15} cm^{-2}, and that the thickness *is saturated after* the dosage of ~10^{15} cm^{-2} [38].

Before the analysis of the Re 4*f* spectra modifications for Re-implanted samples, the tests on a reference sample (bulk h-Re^0) were performed in order to estimate the BE of metallic rhenium states (see **figure S2** in Supplementary Material). The h-Re^0 sample was subjected to annealing due to the fact that as-received h-Re^0 sample had a signal coming from the surface contamination. That signal was comparable to the signal from the metallic rhenium and it was not possible to separate rhenium oxides and metallic sub-peaks unambiguously. After the annealing procedure, characterization of the metallic rhenium structure was made, and several intermediate rhenium oxidation states were found to be present at the surface between the $\mathrm{Re_2O_7}$ phase and the bulk rhenium metal, such as Re^{4+}, Re^{2+}, and $Re^{\delta+}$, where $\delta \sim 1$. As it is shown in [39], the stable binary oxides of rhenium are ReO_2, ReO_3 and Re_2O_7, containing rhenium in the 4+, 6+ and 7+ oxidation states, respectively. ReO_3 is not especially stable: it disproportionates upon heating above 400 ºC with Re^{6+} cations turning into Re^{7+} and Re^{4+}. According to the literature data, Re_2O_7 is chemically stable, but sublimes at a relatively low temperature (reported to be in the range of 225–315 ºC) [39]. Nevertheless, contributions from both ReO_3 and Re_2O_7 were found for the examined here h-Re^0 reference sample. Finally, ReO_2 is stable against disproportionation up to 850 ºC but remains at the surface of the reference sample also after annealing. Ultimately, the BE of the metallic rhenium $4f_{7/2}$ line was identified to be equal to 40.15 eV. Re 4*f* region has well separated spin-orbit component, $\Delta_{Re}{}^0 = 2.43$ eV, with full width at half maximum (FWHM) of lines at 0.35 eV. The observed asymmetry of Re^0 peaks shape (see **figure S2** in Supplementary Material) is due to the interaction of the emitted photoelectron with the conduction electrons in metallic samples. These *shake-up* like events generate a tail on the higher BE side of the main peak instead of discrete shake-up satellites [40, 41]. The obtained results for the metallic rhenium Re 4*f* states allow for the following qualitative analysis of the data presented in **figure 2 (b)**. The BE of the Re $4f_{7/2}$ line for the samples with different implantation doses is the same. The investigated line is shifted by 0.13 eV to higher BE as compared to Re^0. Since the difference of ±0.1 eV may be due to the determination of the zero-point on the energy scale (so-called calibration procedure), it was suggested that Re-ions are bonded to themselves in the implanted samples before the RTA. This means that clustering of rhenium atoms in silicon subnet takes place. Such conclusion agrees well with the RBS results presented in previous section. It should be also noted that before the RTA, Re 4*f* lines show a substantial broadening of their FWHM from 0.35 eV for the metallic rhenium to 0.85 eV for the Re-implanted silicon samples. This broadening could be explained by a few factors: (i) high level of structural disorder expected due to implantation treatment which influences the valence electron charge distribution fluctuation of atoms both in crystalline and close to supposedly amorphous phases (see further discussion concerning modification of Si 2*p* states); (ii) an increase in the Re density of states (DOS) at the Fermi level is possible to occur (it is known that an increase of the DOS at the Fermi edge leads to an increased asymmetry of the core level lines due to the response of the conduction electrons to the creation of the photohole [42]); and (iii) other phases could possibly form (like silicides, etc.) that are able to contribute additionally.

3.3 Modification of Si 2p and Re 4f states due to RTA treatment by means of XPS

The RTA resulted in an incomplete annealing of the radiation defects, especially for the sample with the higher implantation dose. It is reflected in the behavior of $Si^{(el.)}$ 2*p* line, i.e., the estimated BE value is very close to the one for elemental silicon, however, spin-orbit interaction is still unclear for the sample with the higher implantation dose (see region marked $Si^{(el.)}$ in **figure 2** (a)). This may be a consequence of inclusions of Si-Re phases (silicides), Si_xRe_{1-x}, those are likely to be formed, or/and influence of silicon 'surface contribution', that, in turn, perturbed the Si crystalline structure. On the other hand, the BE of Re $4f_{7/2}$ peak after the RTA is shifted to higher values, namely, for 0.68 and 0.85 eV relative to metallic rhenium BE (40.15 eV) for the samples with lower and higher implantation doses, respectively (see **figures 2** (b) and **3** (a, b)). Spin-orbit interaction for both samples is the same and is equal to that of pure metallic rhenium, whereas value of FWHM is the same but is equal to that of implanted samples before the RTA (~0.85 eV). Angle-resolved (AR) XPS data analysis for both samples after the RTA shows that rhenium ions have a similar chemical nature in depth, but their content is different for different doses (see **figure 3**). A few possible explanations could be proposed for such observations. The first possibility would be a formation of Si_xRe_{1-x} solution: according to the results in [43], the rhenium-rich Re_xSi is characterized by a shift of +0.3 eV in BE in Re 4*f* compared to the peak position of the metallic rhenium. The second possibility could be related to a formation of Si-Re phases (silicides). Finally, an influence of silicon atoms on a surface of eventually pure rhenium clusters of small size (below 5 nm) or so-called core-shell structures could also be manifested in such observations. Considering the last possibility and remembering the assumption that in the Re-implanted samples nanoinclusions are present, one can make a working hypothesis that nanoinclusions of larger sizes are formed in the surface layer (up to 10 nm) of the sample with the lower dose. The opposite is true for the sample with the higher dose, where nanoinclusions of smaller sizes are presumably formed. If that is true, then the number of silicon atoms on the surface of a larger inclusion (lower dose) will be smaller than the number of silicon atoms on the surface of a smaller inclusion (higher dose). Effectively, one should expect smaller BE shift, compared to the pure rhenium phase, for Re $4f_{7/2}$ state for the lower implantation dose sample and bigger for the sample with higher implantation dose. This is exactly what is visible in the XPS experimental data in **figure 3**. To verify all the mentioned possibilities (and therefore the hypothesis), subsequent XRD and TEM studies were performed and are discussed in the next sections.

3.4 Examination of the structural characteristics before and after RTA

The crystal structure of the rhenium implanted silicon samples with different rhenium implantation doses before and after the RTA was determined by XRD. The XRD measurements of the samples before the RTA correspond to pure silicon phase (c-Si wafer) shown in **figure 4** (marked as ‘no RTA’), whereas the Si 200 basis-forbidden reflection caused by multiple diffraction [44] and artefact associated with the semiconductor detector are marked “Si 200” and “det”, respectively. No other additional diffraction peaks are seen within the scanning range from 20 to 65 degrees of 2θ. Therefore, the samples before the RTA are assumed to either have a high degree of structural disorder *or/and* be nano-crystalline in nature. This conclusion matches well the results of the RBS and XPS presented above both indicating the formation of highly disordered layer of rhenium, structurally close to amorphous or nano-crystalline. After the RTA, the XRD patterns were collected for both samples again (‘RTA’ in **figure 4**). For the higher implantation dose sample, the XRD pattern includes two new peaks. With high probability these peaks can be associated with the orthorhombic $ReSi_2$ phase [45] (space group: *Immm*) marked in **figure 4** as $ReSi_2$. The broad width of the peaks points to both irregular grain size and grain microstructure. No other reaction products were detected after the RTA, what could indicate that Re doped silicon was stabilized into $ReSi_2$ phase under high temperature (at least for the temperature range studied in this work). However, at this stage the authors cannot exclude existence of even pure rhenium or some silicide inclusions in the examined samples with the size inclusions at the level of 5 nm or smaller that would be invisible to conventional XRD.

3.5 Inclusions size, space distribution, EDS elemental mapping characterization

TEM investigations were performed for both samples after they were subjected to the RTA. The TEM (**figure 5** (a)) and the HAADF STEM (**figure 5** (c)) images reveal the penetration depth of Re ions in Si host matrix to be at the level of 60 nm for the sample with the lower dose, whereas it is further down but less than 80 nm for the sample with the higher dose (see **figure 6** (a, c)). Cross-sectional HR TEM images for the investigated samples and their corresponding SAED patterns are presented in **figures 5** (b, d) and **6** (b, d). The analysis shows presence of hexagonal metallic rhenium and rhenium silicide phases along with a cubic silicon phase marked in **figures 5** and **6** (d).

Figures 5 (e-h) and **6 (e-h)** show the results of STEM and EDS elemental mapping for the investigated samples. High intensity of Re signal is observed in the places of big inclusions (**figures 5** (f) and **6** (f)). This fact indicates that pure rhenium phase exists inside big clusters. Signal from oxygen is clearly seen only at the surface regions (**figures 5** (g) and **6** (g)). That observation agrees well with the analysis of HR XPS Si 2*p* states, **figure 2** (a), that determined silicon-oxide fraction only at the outermost samples’ surface. Consequently, oxygen is absent in the samples’ volume and does not bond to atoms of rhenium. It is worth noting that there are some intensity fluctuations for the silicon signal in the sample with the smaller dose (see **figure 5** (h)). Darker regions correspond to spaces between clusters or close to their boundaries. We suggest that such regions could be explained by the formation of silicides inside of them.

As for the sample with the higher dose, the Re inclusions are poorly visible on the corresponding TEM image, **figure 6** (b). It is related to the occurrence of numerous stacking faults or micro-twins on {111} Si planes. However, the inclusions are visible well in Z-contrast of HAADF STEM image, **figure 6** (e). The interpretation of the SAED patterns, shown in **figure 6** (d), requires presence of the same phases/compounds with the same crystalline structure as in the sample with the lower dose.

Analysis of histograms of size distribution of the inclusions for both samples reveals significant differences in the sizes of nanoinclusions in the Si matrix between the samples with higher and lower doses of implantation (see **figure S3** in Supplementary Material). Namely, no large particles (with a size above 20 nm) were observed in the sample with the higher implantation dose whose size (diameter) of the inclusions exhibited a unimodal distribution, whereas the distribution of inclusions in the sample with the lower dose was bimodal. Such observation agrees with the previous hypothesis based on XPS data analysis.

3.6 Mutual discussion of the electronic and crystallographic structure results supported by DFT

Overall, we found that the implantation of rhenium ions into c-Si matrix results in a modified surface layer with magnetic properties different from those obtained for the samples before the RTA. The RTA at 1000 ^{o}C in argon atmosphere for 60 s leads to noticeable changes in the structural and magnetic properties depending on rhenium fluence. The structural damage induced on the silicon host matrix during implantation is only partially removed. Supposedly, the depth contribution of the implanted species is affected by the out-diffusion process. For the investigated fluencies of rhenium implantation the evidence of aggregates formation is clearly seen both before and after the RTA. The diffractograms before the RTA are similar and reveal only the diffraction peaks of silicon. After the RTA only the sample with the higher dose could have a, presumably, $ReSi_2$ phase which, however, was not detected by both XPS and TEM. No new phases were detected for the sample with the lower dose. The XPS Re 4*f* and Si 2*p* core-level spectra for pure phases (h-Re and c-Si) and $ReSi_2$ where examined in [46]. These rhenium and silicon core-levels were found to have the same BEs in the pure phases as in $ReSi_2$ within experimental errors estimated to be ± 0.1 eV. In the rhenium implanted samples the Re $4f_{7/2}$ level shifts with respect to pure rhenium reference for 0.68/0.85 eV for the lower/higher implantation dose, respectively. Consequently, such an observation means that at the depth of about 10 nm from the surface of the samples the environment for the implanted Re atoms in silicon host matrix is different than the environment in $ReSi_2$ phase. Taking into account possible formation of Si_xRe_{1-x}, c-ReSi, h-ReSi, or an influence of surface silicon atoms on eventually pure rhenium nanoclusters (suggested from analysis of XPS spectra and supported by TEM data analysis), the DFT calculations were aimed to shed light on this. Obtained data are summarized in **Table 1**. The binging energy of Re $f_{7/2}$ peak of metallic rhenium was estimated to be 40.502 eV. This value is in close agreement but still greater than the experimental one of +0.35 eV. Thus, the relative changes in the positions of the Re $4f_{7/2}$ line of selected models to metallic rhenium are followed only. Generally, the gradual addition of silicon atoms to the rhenium leads to a successive shift of the Re $4f_{7/2}$ state towards higher BEs. For instance, substitution of six rhenium atoms by silicon in rhenium lattice (this corresponds to h-$Re_{0.88}Si_{0.12}$ in **Table 1**) gives the BE of 40.586 eV. Subsequent calculation based on hexagonal Re(1)Si(1) model gives the BE at 40.738 eV, whereas for cubic Re(1)Si(1) model this value is 40.568 eV. Consequently, the biggest BE shift when compared to metallic h-Re is for h-ReSi model and it is equal to 0.235 eV. For c-ReSi model this value is just 0.065 eV. The relative difference of calculated BEs for c-ReSi and h-ReSi models is 0.17 eV. If this value is correct, then the conclusion is not encouraging, since the sensitivity of the BE determination in our experiments is practically the same, i.e. 0.15 eV. It makes impossible to unambiguously determine the mentioned above phases by XPS data analysis, but it could be an explanation for higher FWHM for investigated samples when compared to metallic rhenium one. Another observation comes from the fact that according to TEM investigations an average size (diameter) of small inclusions formed in the surface region (up to 10 nm in depth) is 2.2 nm versus 2.7 nm for the samples with the higher and lower fluencies, respectively. A rough estimation of the number of surface silicon atoms on the core of pure rhenium inclusion results in 31 and 26 percent for smaller and bigger inclusions, respectively. Such a result leads us to the conclusion that the RTA treatment of the samples brings a stronger intermixing of rhenium atoms with the host matrix and results in rhenium rich inclusions. One cannot, however, exclude a possibility of existence for core(Re^0)-shell($Re_{1-x}Si_x$) structures. More detailed TEM analysis has to be performed to clarify this issue.

3.7 Magnetic properties results: degree of magnetic nanoinclusions interaction

The magnetic measurements of the samples point to a strong interaction between formed nanoinclusions for both samples. The samples' responses to the external field, $M(H)$, at a constant temperature (2 K and 300 K) are shown in **figure 7**. It is clear that both Re-implanted silicon samples before the RTA exhibit a sizable nonlinear $M(H)$ even at 300 K, saturating clearly just below 10 kOe (see inset in **figure 7**). The RTA increased the magnetic responses in both systems (see **figure 7**).

Before the RTA, a disproportional increase of magnetic properties with dosage is attributed to implanted Re that aggregates into clusters rather than distributes randomly over the host (this was suggested by RBS/c along with XPS examinations and finally confirmed by TEM investigations). Interestingly, the magnetic moment of the sample with the lower dose increased nearly 20-fold after the RTA. This is much greater than the increase observed in the sample with the higher dose, for which a 3-fold increment is observed. As a result, the sample with the lower dose shows nearly two times stronger magnetic response than the sample with the higher dose (see **figure 7**).

Our TEM data showed that after the RTA, the sample with the lower dose exhibits bimodal distribution of nano-aggregates (or particles) as opposed to the sample with the higher dose that has unimodal distribution. Assuming that the number of particles is known, an attempt to fit experimental curves with a standard Langevin expression led to a significant underestimation of the observed magnetic moment in both cases. This leads to the conclusion that both samples are not in a superparamagnetic state *per se* but a great degree of interaction exists between these magnetic nanoinclusions [47, 48]. Moreover, a much higher magnetic moment is attributed to bigger inclusions (≥ 20nm). Based on the results of the RBS/c, XPS, and TEM analysis, it could be concluded that a large portion of implanted Re ions belongs to smaller nanoinclusions, supposedly with c-ReSi and h-ReSi phases, and big inclusions being in pure Re phase.

4. Conclusions

The silicon single crystal was implanted by rhenium ions at room temperature with fluencies of 5×10^{16} and 1×10^{17} at./cm^2. Based on the results of RBS/c and XPS data, it seems that the implantation conditions transform the surface region with a strongly perturbed silicon lattice. The structural property, electronic density, and magnetic properties of examined samples point to aggregation of rhenium ions inside the host matrix that persists after the RTA with different effects on the samples depending on implantation doses. For both implantation doses the results show that the RTA promotes the incorporation of formed aggregation of rhenium ions (inclusions of rhenium rich $Re_{1-x}Si_x$ or c/h- ReSi) distributed closer to the sample's surface (about 10 nm) with surrounding host matrix. As a result, the shift of 4*f* Re core level for +0.68 (the sample with the lower dose) and +0.85 eV (the sample with the higher dose) with respect to pure rhenium is detected. Significant differences were found in the size of distribution of nanoinclusions in the Si matrix for the samples with the higher and smaller implantation doses. No large particles (with diameters above 20 nm) were observed in the sample with the higher dose and the diameters of smaller inclusions, that form unimodal distribution, are up to 12 nm. Moreover, that sample reveals the occurrence of numerous stacking faults or micro-twins on {111} Si planes, thus higher structural disorder. At the same time, the distribution of inclusions in the sample with the lower dose is bimodal (small inclusions with up to 10 nm in diameter and larger ones with diameters around 20-30 nm) and tructural disorder is much weaker. Overall, the samples display a super-spin glass or super-ferromagnetic behavior which gets stronger after the RTA. The nanoinclusions are not detected by conventional XRD measurements, but are predicted by RBS/c and XPS, and are confirmed by TEM investigations.

Ion implantation seems to be a promising technique intended for production of systems of nanoinclusions embedded in a semiconducting matrix. Our results point to the possibility of tuning nanoinclusions size and magnetic properties by adequately controlling the implantation conditions and annealing treatments. The development of this technique in order to produce systems of possible technological relevance will depend on further experimental work and efforts to systematize the results of different implantation conditions.

Acknowledgments

The authors thank Dr. O.A. Bureyev of Institute of Electrophysics, Ural Branch, Russian Academy of Science, Yekaterinburg, Russia, and Dr. A.F. Zatsepin of M.N. Miheev Institute of Metal Physics of Ural Branch of Russian Academy of Sciences, Yekaterinburg, Russia, for providing samples. The authors also thank Dr. A. Sobiesierski of Cardiff University, Cardiff, U.K., for performing chemical etching of the samples. The work was partially supported by the Interdisciplinary Centre for Mathematical and Computational Modelling (ICM) at University of Warsaw, Poland.

References

[1] H. Ohno, M.D. Stiles, B. Dieny, Spintronics *Proc. IEEE Inst. Electr. Electron. Eng.* 104 (**2016**) 1782.

[2] M. Tanaka, S. Ohya, P.N. Hai, Recent progress in III-V based ferromagnetic semiconductors: Band structure, Fermi level, and tunneling transport *Appl. Phys. Rev.* 1 (**2014**) 011102.

[3] Functional Materials. 1st Edition, Preparation, Processing and Applications, S. Banerjee, A.K. Tyagi, Eds.; Elsevier, **2011**; ISBN: 978-0-12-385142-0.

[4] T. Dietl, H. Ohno, Dilute ferromagnetic semiconductors: Physics and spintronic structures *Rev. Mod. Phys.* 86 (**2014**) 187.

[5] G. Kunert, S. Dobkowska, T. Li, H. Reuther, C. Kruse, S. Figge, R. Jakieła, A. Bonanni, J. Grenzer, W. Stefanowicz, J. von Borany, M. Sawicki, T. Dietl, D. Hommel, $Ga_{1-x}Mn_xN$ epitaxial films with high magnetization *Appl. Phys. Lett.* 101 (**2012**) 022413.

[6] M. Bolduc, C. Awo-Affouda, A. Stollenwerk, M.B. Huang, F.G. Ramos, G. Agnello, V.P. LaBella, Above room temperature ferromagnetism in Mn-ion implanted Si *Phys. Rev. B* 71 (**2005**) 033302.

[7] J. Chen, F. Luo, T. Li, Z. Zheng, S. Jin, Z. Yang, L. Guo, C. Liu, Effect of annealing temperature on the ferromagnetism of Co-implanted silicon *Nucl. Instrum. Method. Phys. Res. B: Beam Interactions with Materials and Atoms* 307 (**2013**) 404.

[8] Y.D. Park, A.T. Hanbicki, S.C. Erwin, C.S. Hellberg, J.M. Sullivan, J.E. Mattson, T.F. Ambrose, A. Wilson, G. Spanos, B.T. Jonker, A Group-IV Ferromagnetic Semiconductor: Mn_xGe_{1-x} *Science* 295 (**2002**) 651.

[9] W. Zhang, L. Guo, G. Peng, T. Li, S. Feng, Z. Zhou, T. Peng, Z. Quan, Effect of annealing temperature on magnetic property of $Si_{1-x}Cr_x$ thin films *Thin Solid Films* 520 (**2011**) 769.

[10] T. Dietl, K. Sato, T. Fukushima, A. Bonanni, M. Jamet, A. Barski, S. Kuroda, M. Tanaka, P. Nam Hai, H. Katayama-Yoshida, Spinodal nanodecomposition in semiconductors doped with transition metals *Rev. Mod. Phys.* 87 (**2015**) 1311.

[11] D. Recht, M.J. Smith, S. Charnvanichborikarn, J.T. Sullivan, M.T. Winkler, J. Mathews, J.M. Warrender, T. Buonassisi, J.S. Williams, S. Gradečak, M.J. Aziz, Supersaturating silicon with transition metals by ion implantation and pulsed laser melting *J. Appl. Phys.* 114 (**2013**) 124903.

[12] E. García-Hemme, R. García-Hernansanz, J. Olea, D. Pastor, A. del Prado, I. Mártil, G. González-Díaz, Far infrared photoconductivity in a silicon based material: Vanadium supersaturated silicon *Appl. Phys. Lett.* 103 (**2013**) 032101.

[13] M. Wierzbowska, A. Fleszar, Density functional theory calculations for a single Re impurity in silicon *Phys. Rev. B* 83 (**2011**) 184418.

[14] Wierzbowska, M. Poisoning of magnetism in silicon doped with Re, caused by a charge transfer from interstitials to substitutionals, by means of the self-interaction corrected density-functional approach *J. Appl. Phys.* 2012, 112, 013919.

[15] M. Wierzbowska, Exchange interactions and T_c in rhenium-doped silicon: DFT, DFT + U and Monte Carlo calculations *J. Phys.: Condens. Matter.* 24 (2012) 126002.

[16] H. Ohno, Making Nonmagnetic Semiconductors Ferromagnetic *Science* 281 (**1998**) 951.

[17] S. Kahwaji, W. Bowman, M.D. Robertson, T.L. Monchesky, The influence of a Pb surfactant on the magnetism of dilute $Si_{1-x}Mn_x$ films *J. Appl. Phys.* 113 (**2013**) 063910.

[18] K. Potzger, Ion-beam synthesis of magnetic semiconductors *Nucl. Instrum. Method. Phys. Res. B* 272 (**2012**) 78.

[19] Y.L. Soo, J.H. Yao, C.S. Wang, S.L. Chang, C.A. Hsieh, J.F. Lee, T.S. Chin, Local structures and concentration dependence of magnetic properties in Cr- and Mn-doped amorphous silicon ferromagnetic thin films *Phys. Rev. B* 81 (2010) 104104.

[20] J.A. Gardener, I. Liaw, G. Aeppli, I.W. Boyd, R.J. Chater, T.S. Jones, D.S. McPhail, G. Sankar, A. Marshall Stoneham, M. Sikora, G. Thornton, S. Heutz, A novel route for the inclusion of metal dopants in silicon *Nanotechnology* 21 (**2010**) 025304.

[21] F.J. Rueß, M. El Kazzi, L. Czornomaz, P. Mensch, M. Hopstaken, A. Fuhrer, Confinement and integration of magnetic impurities in silicon *Appl. Phys. Lett.* 102 (2013) 082101.

[22] M.M. Otrokov, A. Ernst, V.V. Tugushev, S. Ostanin, P. Buczek, L.M. Sandratskii, G. Fischer, W. Hergert, I. Mertig, V.M. Kuznetsov, E.V. Chulkov, Ab initio study of the magnetic ordering in Si/Mn digital alloys *Phys. Rev. B* 84 (**2011**) 144431.

[23] A.R. Wildes, J. Mayer, K. Theis-Bröhl, The growth and structure of epitaxial niobium on sapphire *Thin Solid Films* 401 (**2001**) 7.

[24] S. Oh, D.A. Hite, K. Cicak, K.D. Osborn, R.W. Simmonds, R. McDermott, K.B. Cooper, M. Steffen, J.M. Martinis, D.P. Pappas, Epitaxial growth of rhenium with sputtering *Thin Solid Films* 496 (**2006**) 389.

[25] T.V. Kulevoy, N.N. Gerasimenko, D.N. Seleznev, P.A. Fedorov, A.A. Temirov, M.E. Alyoshin, S.V. Kraevsky, D.I. Smirnov, P.E. Yakushin, V.V. Khoroshilov, Rhenium ion beam for implantation into semiconductors *Rev. Scientif. Instrum.* 83 (**2012**) 02B913.

[26] Silicon-based Spintronic Materials, Liam Damewood, C.Y. Fong, L.H. Yang, Eds.; World Scientific Book, 2014; LLNL-BOOK-659524.

[27] Gavrilov N. V., Oks E. M., High-Current Pulse Sources of Broad Beams of Gas and Metal Ions for Surface Treatment, *Nuclear Instruments and Methods in Physics Research Section A* 2000, 439, 31.

[28] N. Fairley, Casa Software Ltd, Software Package for the Analysis of XPS Results, CasaXPS version 2.3.17dev6.6o, http://www.casaxps.com

[29] I.N. Demchenko, W. Lisowski, Y. Syryanyy, Y. Melikhov, I. Zaytseva, P. Konstantynov, M. Chernyshova,; M.Z. Cieplak, Use of XPS to clarify the Hall coefficient sign variation in thin niobium layers buried in silicon *Appl. Surf. Sc.* 399 (**2017**) 32.

[30] M. Sawicki, W. Stefanowicz, A. Ney, Sensitive SQUID magnetometry for studying nanomagnetism *Semicond. Sci. Technol.* 26 (**2011**) 064006.

[31] K. Blaha, G.K.H. Schwarz, D. Madsen, J. Kvasnicka, Luitz, WIEN2k, an Argmented Plane Wave + Local Orbitals Program for Calculating Crystal Properties, Karlheinz Schwarz, Techn. Universitat Wien, Austria, **2001**; ISBN 3-9501031-1-2.

[32] P. Perdew, K. Burke, M. Ernzerhof, Generalized Gradient Approximation Made Simple *Phys. Rev. L* 77 (**1996**) 3865.

[33] A.T. Paxton, A.J. Craven, J.M. Gregg, D.W. McComb, Bandstructure approach to near edge structure *J. Microscopy* 210 (**2003**) 35.

[34] J.F. Ziegler, SRIM - The Stopping and Range of Ions in Matter, http://www.srim.org/

[35] M. Szabadi, P. Hess, Elastic and mechanical properties of ion-implanted silicon determined by surface-acoustic-wave spectrometry *Phys. Rev. B* 58 (1998) 8941.

[36] L. Nowicki, A. Turos, R. Ratajczak, A. Stonert, F. Garrido, Modern analysis of ion channeling data by Monte Carlo simulations *Nucl. Instr. Meth. Phys. Res. B* 240 (**2005**) 277.

[37] Z.H. Lu, A. Yelon, Static charge fluctuations in -implanted silicon *Phys. Rev. B* 41 (**1990**) 3284.

[38] M. Ishii, Y. Hirose, T. Sato, T. Ohwaki, Y. Taga, In situ analysis of Si(100) surface damage induced by low-energy rare-gas ion bombardment using x-ray photoelectron spectroscopy *J. Vac. Sci. Technol. A* 15 (**1997**) 820.

[39] M.T. Greiner, T.C.R. Rocha, B. Johnson, A. Klyushin, A. Knop-Gericke, R. Schlögl, The Oxidation of Rhenium and Identification of Rhenium Oxides During Catalytic. Partial Oxidation of Ethylene: An In situ XPS Study *Z. Phys. Chem.* 228 (**2014**) 521.

[40] D. Briggs, XPS: Basic Principles, Spectral Features and Qualitative Analysis, in: D. Briggs, J.T. Grant Eds.; Surface Analysis by Auger and X-ray Photoelectron Spectroscopy, IM Publications, Chichester, **2003**; 31.

[41] I.N. Demchenko, Y. Syryanyy, Y. Melikhov, L. Nittler, L. Gladczuk, K. Lasek, L. Cozzarini, M. Dalmiglio, A. Goldoni, P. Konstantynov, M. Chernyshova, X-ray photoelectron spectroscopy analysis as a tool to assess factors influencing magnetic anisotropy type in Co/MgO system with gold interlayer *Script. Mater.* 145 (**2018**) 50.

[42] G.K. Wertheim, P.H. Citrin Photoemission in Solids I (Springer Topics in Applied Physics 26) L. Ley, M. Cardona, Eds.;'Berlin: Springer, **1979**.

[43] R. Reiche, S. Oswald, K. Wetzig, XPS and factor analysis for investigation of sputter-cleaned surfaces of metal (Re, Ir, Cr)–silicon thin films *Appl. Surf. Science* 179 (**2001**) 316.

[44] P. Zaumseil, High-resolution characterization of the forbidden Si 200 and Si 222 reflections *J. Appl. Cryst.* 48 (**2015**) 528.

[45] T. Siegrist, F. Hulliger, G. Travaglini, The crystal structure and some properties of $ReSi_2$ *J. Less-Common Met.* 92 (**1983**) 119.

[46] T.A. Nguyen Tan, J.Y. Veuillen, P. Muret, S. Kennou, A. Siokou, S. Ladas, F. Lahatra Razafindramisa, M. Brunel, Semiconducting rhenium silicide thin films on Si(111) *J. Appl. Phys.* 77 (**1995**) 2514.

[47] O. Petracic, Superparamagnetic nanoparticle ensembles *Superlatt. Microstruct.* 47 (**2010**) 569.

[48] K. Stojak Repa, D. Israel, J. Alonso, M.H. Phan, E.M. Palmero, M. Vazquez, H. Srikanth, Superparamagnetic properties of carbon nanotubes filled with $NiFe_2O_4$ nanoparticles *J. Appl. Phys.* 117 (**2015**) 17C723.

Table 1. *Position of rhenium 4$f_{7/2}$ line calculated by Wien2k code.*

Model	4$f_{7/2}$ (eV)	displacement relative to the 4$f_{7/2}$ line of metallic rhenium
h-Re^0	40.503	0
h-$Re_{0.88}Si_{0.12}$	40.586	+0.083
h-ReSi	40.738	+0.235
c-ReSi	40.568	+0.065

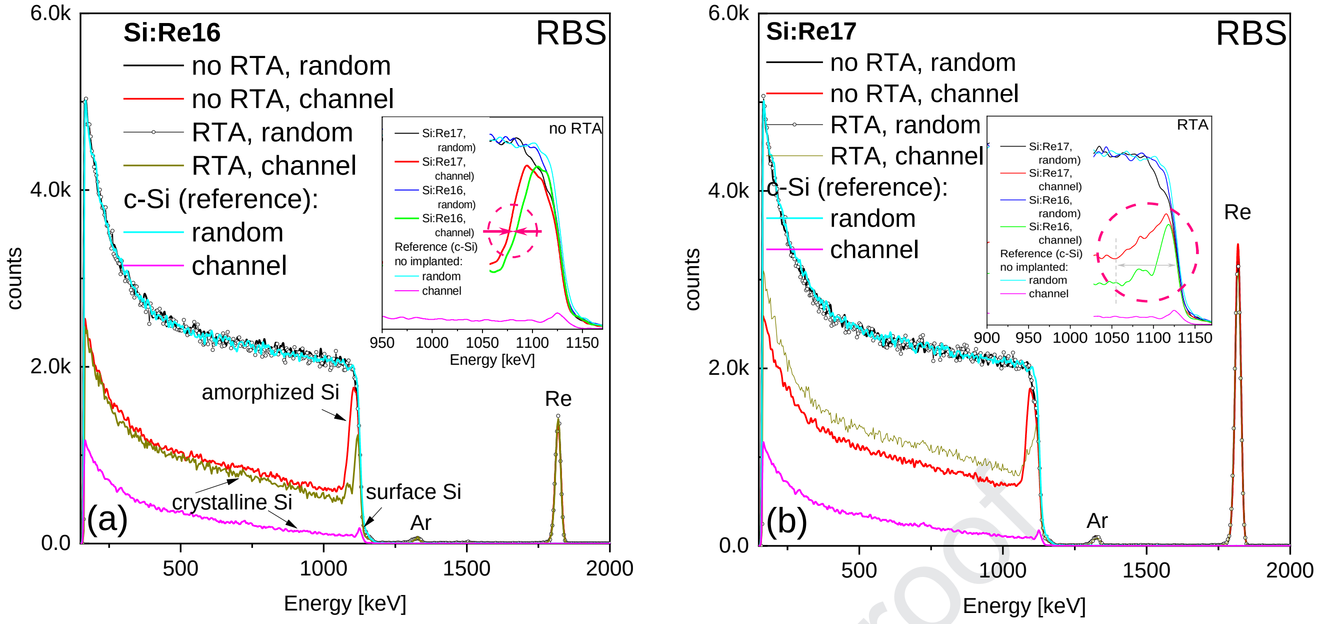

Figure 1. (color online) Channeling and random RBS spectra (before and after RTA treatment) from Re-implanted silicon with dose: (a) 5×10^{16} ions/cm^2; (b) 1×10^{17} ions/cm^2. The insets show the difference of the damaged Si surface layer thickness for samples with different implantation doses and annealing treatments.

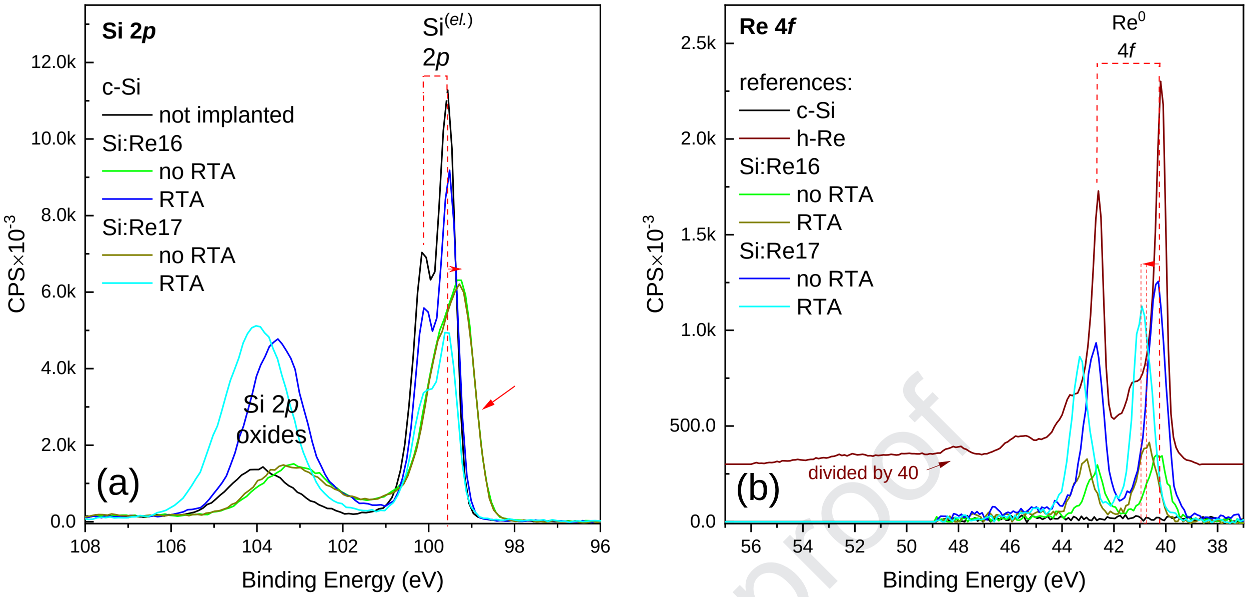

Figure 2. (color online) (a) Comparison of HR XPS Si 2*p* spectra of a reference silicon (c-Si) and of samples with different doses of Re (Si:Re16 and Si:Re17 before and after RTA); (b) Re 4*f* states of implanted samples with different doses (Si:Re16 and Si:Re17 before RTA and after RTA) compared to metallic rhenium (h-Re, after surface cleaning). Spectrum of c-Re was vertically shifted for clarity.

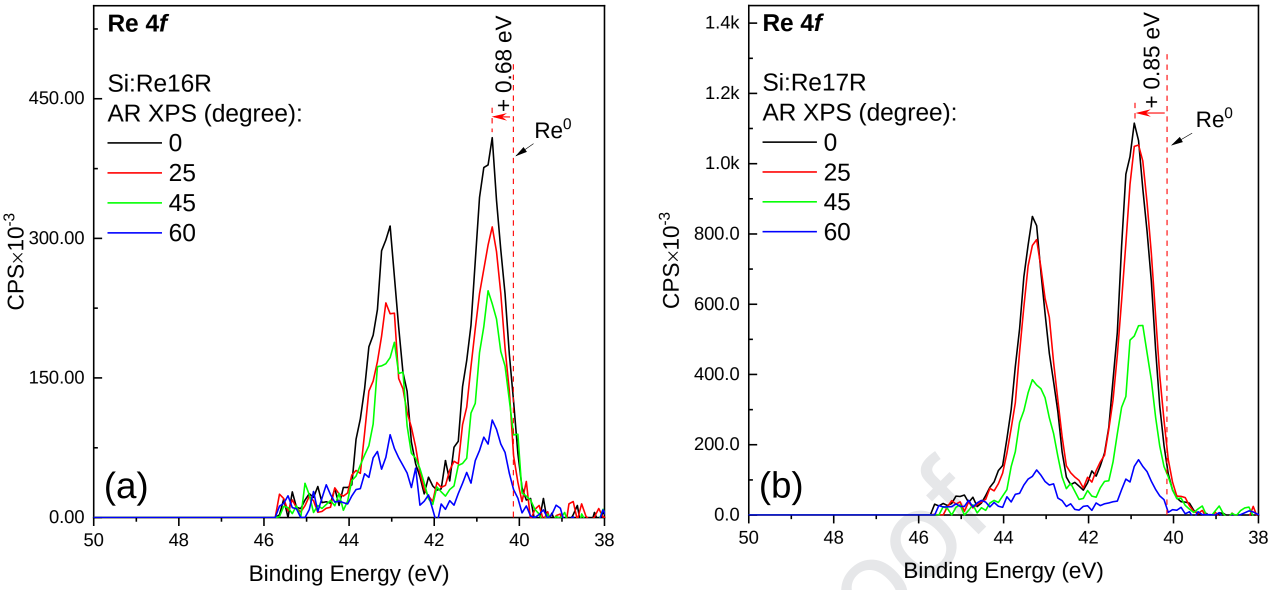

Figure 3. (color online) AR XPS Re 4*f* spectra for Re-implanted silicon after RTA: (a) implantation dose: 5x10^{16} ions/cm^2; (b) implantation dose: 1x10^{17} ions/cm^2.

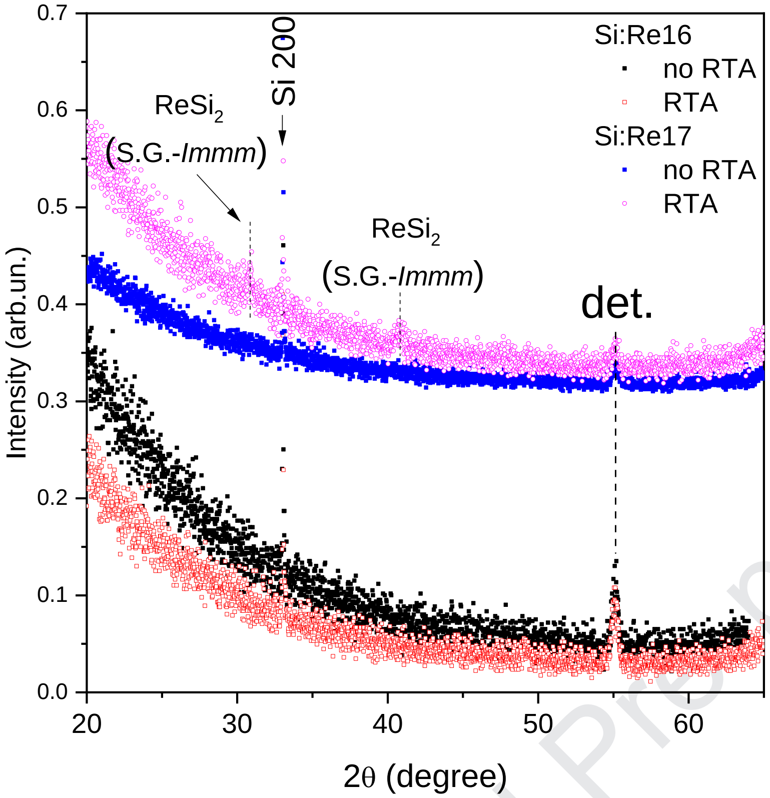

Figure 4. (color online) X-ray diffraction patterns of Re-implanted silicon before and after RTA for different doses of implantation: 5x10^{16} ions/cm^2; 1x10^{17} ions/cm^2.

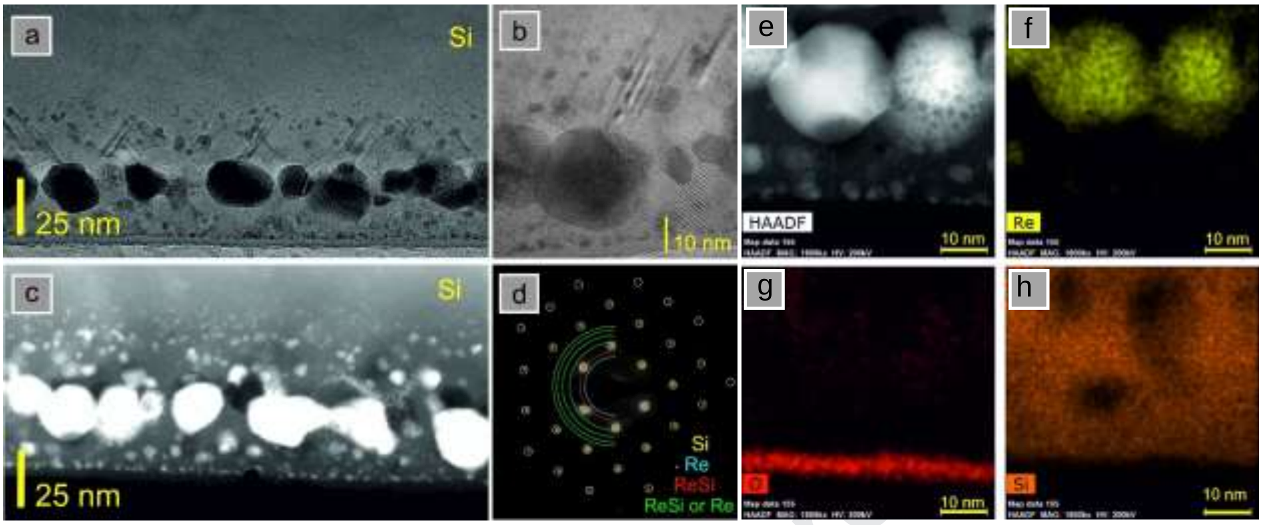

Figure 5. (color online) (a) TEM image of the sample with lower dose of implantation after the RTA. Depth implementation of rhenium in silicon is less than 60 nm. (b) HRTEM of selected area with Re and ReSi inclusions. (c) HAADF STEM image shows morphology of Si:Re16R in Z-contrast. (d) SAED patterns with identified structural phases: c-Si (yellow), Re hexagonal (blue), ReSi cubic (red), and either ReSi-hex or Re-hex phase that cannot be separated (green). (e) HAADF HR-STEM image of the sample with lower dose of implantation after the RTA with EDX maps of (f) Re, (g) O, and (h) Si.

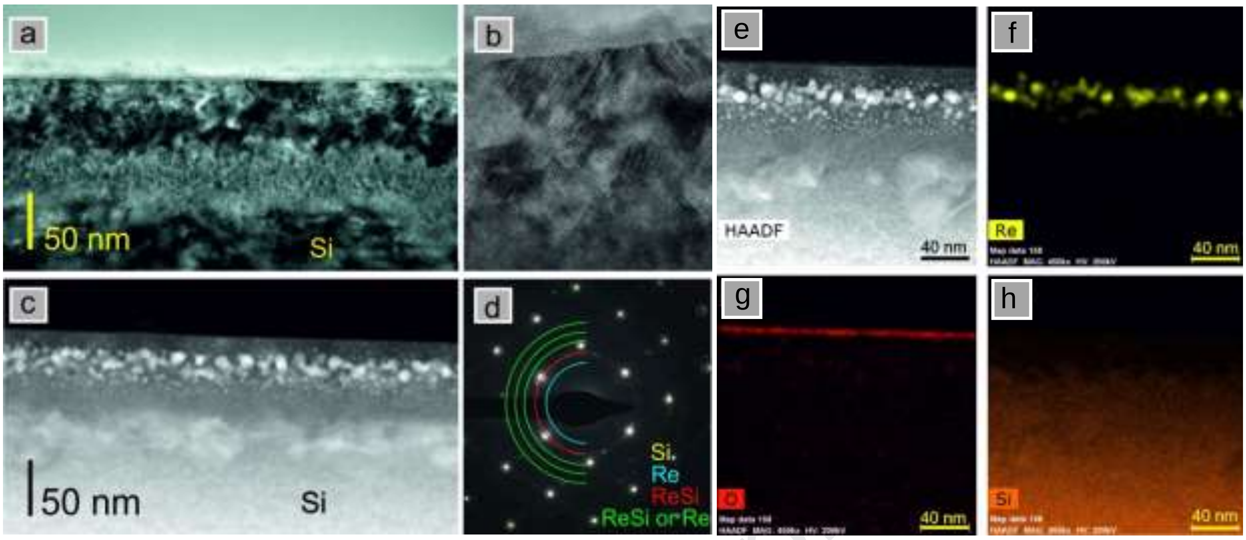

Figure 6. (color online) a) TEM image of the sample with higher dose of implantation after the RTA. Depth implementation of rhenium in silicon is less than 80 nm. b) HRTEM of selected area with Re and ReSi inclusions with visible stacking faults or microtwins on {111} Si planes. c) HAADF STEM image showed morphology of Si:Re17R in Z-contrast. d) SAED patterns with identified structural phases: c-Si (yellow), Re hexagonal (blue), ReSi cubic (red), and either ReSi-hex or Re-hex phase that cannot be separated (green). (e) HAADF HR-STEM image of the sample with higher dose of implantation after the RTA with EDX maps of (f) Re, (g) O, and (h) Si.

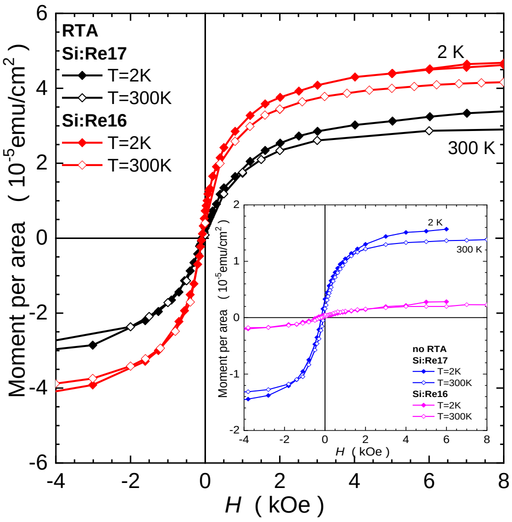

Figure 7. (color online) Magnetic moment as a function of magnetic field for Re-implanted silicon samples with different doses of implantation measured at 2 and 300 K after the RTA treatment (insert shows magnetic moment dependence for the same samples before the RTA). Note that magnetic moment of the sample with the lower dose increased by the factor of about 20 after the RTA, whereas for the sample with the higher dose the factor of 3 only is observed.

Highlights

- The structural, electronic, and magnetic properties of low-energy rhenium implanted c-Si are examined for the first time.
- The analysis of rhenium-depth distribution and channeled RBS spectra using the McChasy code shows that the implanted Re-ions are located in the interstitial lattice positions and suggests bimodal distribution of inclusions in the silicon.
- Complex XPS, DFT simulations, and TEM data analysis allowed to conclude that the near-surface layer of the sample (~10 nm) consist of nanoinclusions with cubic and/or hexagonal ReSi.
- The magnetic response of the examined systems after the RTA indicates a presence of magnetic interactions between the nanoinclusions resulting in the system exhibiting super-spin glass or super-ferromagnetism.

Declaration of Interest Statement

☒ The authors declare that they have no known competing financial interests or personal relationships that could have appeared to influence the work reported in this paper.

☐The authors declare the following financial interests/personal relationships which may be considered as potential competing interests:

As a corresponding author, I sign this form on behalf of all authors.

dr hab. Iraida N. Demchenko
(Corresponding author)
University of Warsaw, Department of Chemistry
ul. Pasteura 1
02-093 Warsaw, Poland
E-mail address:
idemchenko@chem.uw.edu.pl